Surface resonance of the (2 × 1) reconstructed lanthanum hexaboride (001)-cleavage plane: A combined STM and DFT study

P. Buchsteiner [1] F. Sohn,[2,3] J. G. Horstmann,[1] J. Voigt [1] M. Ciomaga Hatnean [4]
G. Balakrishnan,[4] C. Ropers,[1] P. E. Blöchl [3,2] and M. Wenderoth [1,*]

[1]*IV. Physikalisches Institut, Georg-August-Universität Göttingen, 37077 Göttingen, Germany*
[2]*Institut für Theoretische Physik, Georg-August-Universität Göttingen, 37077 Göttingen, Germany*
[3]*Institut für theoretische Physik, Technische Universität Clausthal, 38678 Clausthal-Zellerfeld, Germany*
[4]*Department of Physics, University of Warwick, Coventry CV4 7AL, United Kingdom*

We performed a combined study of the (001)-cleavage plane of lanthanum hexaboride (LaB$_6$) using scanning tunneling microscopy and density-functional theory (DFT). Experimentally, we found a (2 × 1) reconstructed surface on a local scale. The reconstruction is only short-range ordered and tends to order perpendicularly to step edges. At larger distances from surface steps, the reconstruction evolves to a labyrinthlike pattern. These findings are supported by low-energy electron diffraction experiments. Slab calculations within the framework of DFT show that the atomic structure consists of parallel lanthanum chains on top of boron octahedra. Scanning tunneling spectroscopy shows a prominent spectral feature at -0.6 eV. Using DFT, we identify this structure as a surface resonance of the (2 × 1) reconstructed LaB$_6$ (100) surface which is dominated by boron dangling bond states and lanthanum d states.

I. INTRODUCTION

The rare-earth hexaborides (RB$_6$) are a materials class with a common, relatively simple crystalline structure, but widely tunable electronic and magnetic properties. For example, dense Kondo behavior is found in CeB$_6$ [1], PrB$_6$, and NdB$_6$ order antiferromagnetically [2], SmB$_6$ is a Kondo insulator [3,4], EuB$_6$ is a ferromagnetic semimetal which exhibits colossal magnetoresistance [5], and YbB$_6$ is proposed to host topologically protected states without a Kondo mechanism [6]. The variety of these phenomena can be traced back to the $4f$ occupancy increasing from $4f^0$ for La up to $4f^{14}$ in Lu as the rare-earth elements.

All rare-earth hexaborides share the same cubic crystal structure with the B$_6$ octahedra located at the cube's corners and the rare-earth element at the center, as seen in Fig. 1(a). A three-dimensional covalent binding network between the B$_6$ octahedra can be achieved by electron donation of the rare-earth element, leading to positively charged ions and negatively charged boron cages in the crystal structure [7]. The lattice constant changes only slightly across the RB$_6$ series.

One of the most prominent hexaborides is LaB$_6$, a widely used electron emitter due to its extraordinarily low work function [8]. Recently, there has been a growing interest in its solar heat absorbance with regard to possible applications in solar energy devices [9,10]. Although surface properties play a crucial role in these applications, surface studies of this system display a rather incomplete picture. Even the ground-state geometrical structure of the (001) surface is under current debate. Up to the present date, experimental results show a simple (1 × 1) reconstructed surface [8], as found in low-energy

electron diffraction (LEED) and Auger electron spectroscopy studies [11–17]. Scanning tunneling microscopy (STM) experiments at room temperature and under UHV conditions have shown a (1 × 1) structure, which has been described to be lanthanum terminated [18,19]. However, it should be noted that the samples of the aforementioned studies have been prepared by polishing and heating. Recently, surface slab calculations of LaB$_6$ (001) based on density-functional theory (DFT) have been made [20]. Therein, various surface reconstructions are taken into account. Their prediction is a (2 × 1) reconstructed surface as ground state. These findings seemingly contradict the (1 × 1) surface structure observed so far.

To solve this discrepancy between previous experimental results and recent theoretical predictions, we investigated LaB$_6$ (001) prepared by cleavage in UHV. Therefore, annealing-related impacts on the surface morphology, such as preferential evaporation or thermally activated reorganization, can be minimized.
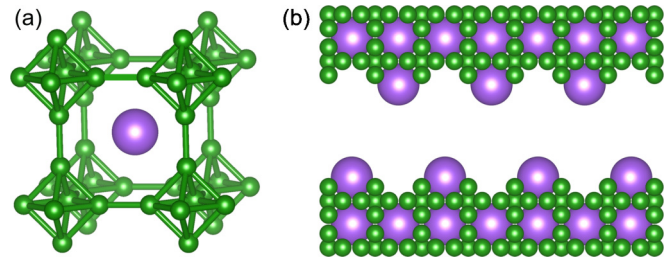

FIG. 1. (a) Crystal structure of RB$_6$, where the rare-earth element is located at the center of the simple cubic unit cell and the B$_6$ octahedra at the corners. (b) Side view of two cleaved surfaces, where each side is partly La terminated.

*Corresponding author: martin.wenderoth@uni-goettingen.de

A (2×1) reconstructed surface is unambiguously found by using high-resolution STM and LEED measurements. DFT slab calculations resolve the chemical nature of the (2×1) reconstruction as parallel rows of lanthanum atoms on top of nonreconstructed B_6 cages. Its electronic structure close to the Fermi energy is governed by a surface resonance, which is mainly composed of boron sp-hybrid dangling bond orbitals.

II. METHODS

A. Experimental techniques

STM experiments were performed in a home-built microscope operating at 8 K and at a base pressure of 4×10^{-11} mbar. Tunneling tips were made by electrochemical etching of polycrystalline tungsten wire. The LaB_6 single crystals were grown using the floating zone technique as described in Refs. [21,22]. The crystals were oriented by gamma-ray diffraction and cut along the (001) plane into rectangular samples of about 1×4 (mm)^2 size and $300\,\mu$m thickness. The samples were cleaved *in situ* at room temperature along the (001) plane followed by immediate transfer to the STM head at cryogenic temperature. All STM images were recorded using the constant current topography (CCT) mode. LEED experiments were performed on identically prepared samples, cleaved at a base pressure of 2×10^{-8} mbar and investigated at 2×10^{-10} mbar. The diffraction images presented in this paper were recorded at either room temperature or at 27 K. For our LEED experiments, we used an ultrafast LEED setup (ULEED), as described in Ref. [23]. This setup features a laser-pulsed electron gun with an electron beam diameter of about $80\,\mu$m at the sample. With this technique, the electron beam contains significantly less electrons than in conventional systems. Thus, the possibility of electron-beam-induced surface damage is drastically reduced. The resulting small number of scattered electrons is detected with a microchannel plate. Atomic force microscopy (AFM) measurements were conducted in a commercial instrument manufactured by Agilent, which operates at ambient condition.

B. Calculations

Theoretical results presented in this paper are based on DFT [24,25] and are obtained with the CP-PAW code [26], which employs the projector-augmented wave method [27] together with a functional minimization scheme derived from the Car-Parrinello molecular dynamics approach [28]. We use the local hybrid exchange-correlation functional PBE0r described elsewhere [29], which locally replaces a fraction of the Perdew-Burke-Ernzerhof (PBE) [30] exchange with the same portion of the exact Hartree-Fock exchange. In the PBE0r functional the Fock-term is expressed in local orbitals and only on-site terms are retained.

III. RESULTS

A. Surface morphology

For most of the encountered surfaces probed by STM, the surface appears rather disordered. This is described in more detail in Appendix A. Atomically ordered areas on LaB_6, as seen in Fig. 2, are scarce and have to be searched for. The
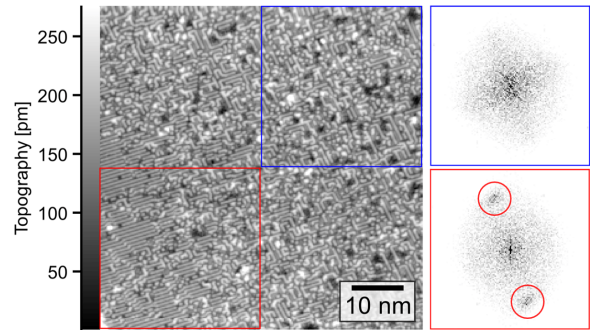

FIG. 2. Atomically resolved CCT taken at 0.8 V/0.1 nA. Atomic rows with a spacing of two bulk lattice constants are present, which are mostly labyrinthlike arranged. The Fourier analysis of a surface area with a rather ordered region shows clear signs of the (2×1) reconstruction, see red-marked area. For most regions no distinct peaks in the Fourier transform can be observed, see blue-marked area.

atomic structure appears chainlike with a spacing of two bulk lattice constants. Hence, (2×1) reconstruction peaks can be clearly observed in the Fourier analysis, as seen for the red-marked area of Fig. 2. However, this (2×1) reconstruction is ordered only on a short range and is mainly labyrinthlike arranged, as seen in the upper right corner of the CCT image in Fig. 2. Although individual chains can still be resolved, no signs of a (2×1) reconstruction can by found in the Fourier analysis due to the lack of long-range order.

A high-resolution image of the (2×1) reconstruction, Fig. 3(a), shows that even for the more ordered areas, the chains exhibit kinks and defects. In the vicinity of the region shown in Fig. 3(a), a step edge of one lattice constant height has been found.

At the step edge, the most ordered (2×1) reconstruction is observed. Farther away from the step, the chains lose their
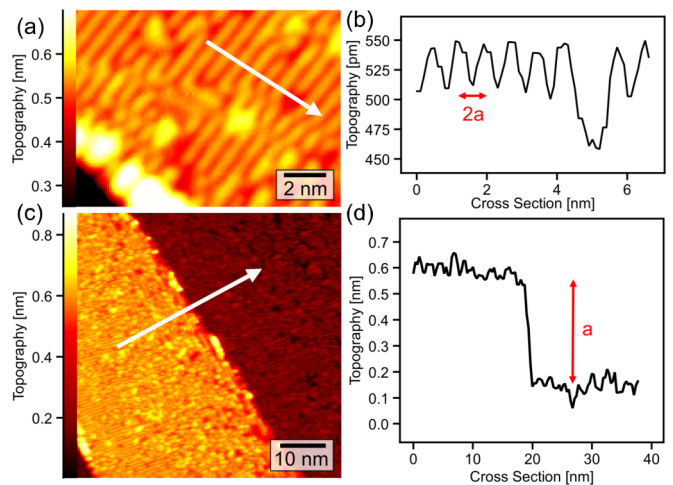

FIG. 3. (a) High-resolution CCT of the (2×1) reconstruction taken at 1 V/0.1 nA. (b) Cross section along the (2×1) reconstruction as indicated by the white arrow in (a). (c) Large scale overview taken at 1 V/0.1 nA in the vicinity of the high-resolution image in (a). (d) The height profile of (c) shows that the step is of about 4.1 Å height, which amounts to one bulk lattice constant a.
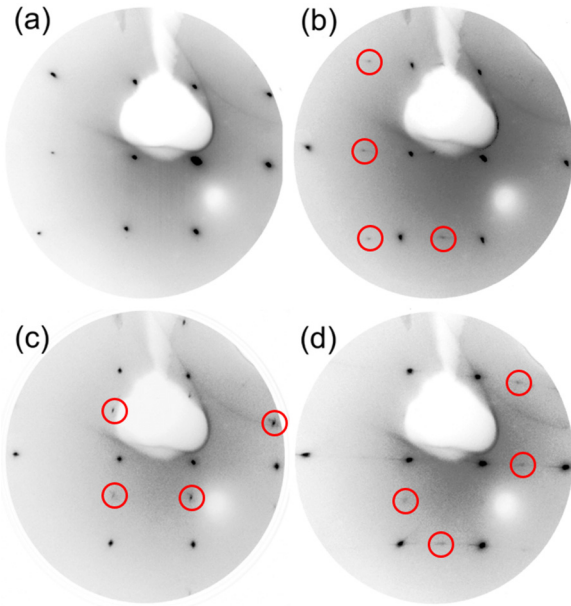
FIG. 4. ULEED images of different locations on the cleaved LaB$_6$ (001) surface. (a) Only (1 × 1) spots are visible, taken at 130 eV and room temperature. In (b), additionally, (2 × 1) spots are present, 100 eV/RT and in (c) (1 × 2) spots are observed, 100 eV/27 K. In (d), both (1 × 2) and (2 × 1) spots are present, 100 eV/27 K. The observed reconstruction spots are marked by red circles.
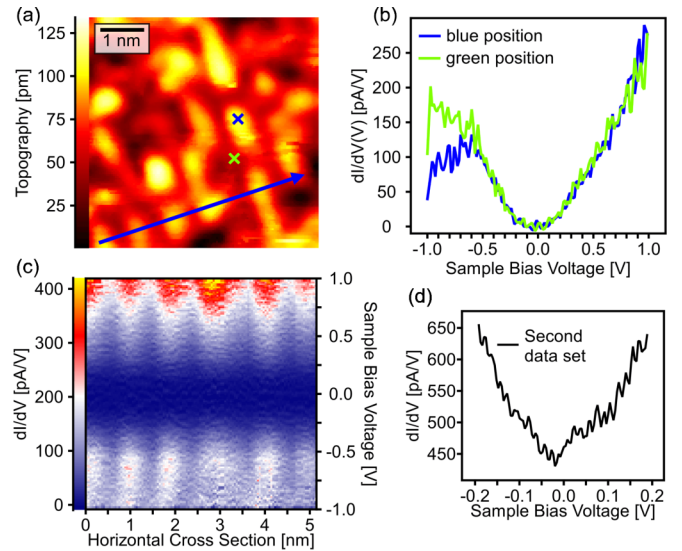

FIG. 5. (a) CCT taken at 1 V/0.1 nA. (b) Two exemplary dI/d$V(V)$ curves obtained from the marked positions are shown. (c) The horizontal arrow in (a) marks the line along the dI/d$V(V)$ cross section was taken, which is shown here. (d) dI/d$V(V)$ curve obtained from a second data set, see Appendix A, to resolve the energy region around E_F.

preferential orientation perpendicular to the step edge, and a more labyrinthlike arrangement is seen, which is similar to the observation in Fig. 2. Therefore, our findings so far suggest a correlation between steps and the occurrence of a well-ordered (2 × 1) reconstruction.

The spatially rather limited observation of long-range order explains why signs of a (2 × 1) reconstruction have not yet been found in LEED experiments. In our standard LEED setup, only a (1 × 1) structure could be seen that vanished after about 30 minutes of measurement time at a pressure of 10^{-9} mbar. The situation changes when using the ultrafast LEED setup and measurements could be carried out over a couple of hours without any noticeable change. Figure 4 sums up the observed diffraction patterns. For most of the sample areas, only a (1 × 1) pattern was found, as seen in Fig. 4(a). In some surface areas, as shown in Figs. 4(b) and 4(c), signs of a (2 × 1) or (1 × 2) reconstruction are present. In one surface region, both (2 × 1) and (1 × 2) spots were observed, as depicted in Fig. 4(d). Note that the diffraction patterns do not change upon cooling the sample down to 27 K, apart from the increasing spot intensity and reduced background noise level due to the temperature-dependent Debye-Waller factor.

To clarify the chemical nature of the (2 × 1) reconstructed surface, scanning tunneling spectroscopy (STS) was carried out.

B. Spatially resolved spectroscopy

Figure 5(a) shows a CCT image, where, simultaneously to the topography, at every measurement point an $I(V)$ curve and the apparent barrier height Φ_{app} were recorded. The chains of

the (2 × 1) reconstruction in Fig. 5 extend for only a few unit cells and are interrupted by various defects. Using the $I(V)$ curve, its differential conductance dI/d$V(V)$ can be seen as an approximation for the local density of states (LDOS) [31,32]. Figure 5(b) shows two dI/d$V(V)$ spectra obtained from the blue- and the green-marked positions. Clearly, a peak in the differential conductance at about −0.6 eV can be resolved on top of the protrusion of the reconstruction, blue-marked position, as well as a steep rise of dI/d$V(V)$ toward positive bias voltages. To visualize the spatial variation of the LDOS, the differential conductance can be plotted position dependent as a color coded dI/d$V(V, x)$ cross section. Since the $I(V)$ curves are recorded quasisimultaneously to the CCT, these curves are taken on a modulated contour line given by the topography. To project the measurement onto a constant height above the surface, a topography normalization is applied, as described in Ref. [33]. This can be done by using the apparent barrier height Φ_{app}, which is defined as [34]

$$\Phi_{app} = \frac{\hbar^2}{8m_e}\left(\frac{d\ln I}{ds}\right)^2. \quad (1)$$

Here, ds is the change of the tip-sample separation and m_e the electron mass. The apparent barrier height is often used as an estimate for the sample work function. However, its absolute value is connected to the work functions of both tip and sample. The spatially resolved $\Phi_{app}(x, y)$ map can be seen in Appendix A, Fig. 12(b), with a mean value of (1.05 ± 0.17) eV. After performing the normalization, the dI/d$V(V, x)$ data reveals that the −0.6 eV peak is strongest at the protrusions of the reconstruction, as seen in Fig. 5(c) for the cross section along the marked direction. However, for this data set, the tunneling current has dropped below 1 pA in the vicinity of the Fermi energy, which could be mistaken

for a nonmetallic surface. To resolve the energy region around E_F, another spectroscopy was performed, which was acquired at a smaller bias voltage set point of 0.2 V. The spatially averaged $dI/dV(V)$-curve can be seen in Fig. 5(d) and the full data set in Appendix A, Fig. 13. A finite conductance at E_F is clearly present. Moreover, the differential conductance has a parabolic shape with a minimum shifted slightly toward negative bias voltages with an additional $dI/dV(V)$ feature at 0.1 eV. The derived apparent barrier height is $\Phi_{app} = (2.99 \pm 0.27)$ eV.

C. Surface simulations

Our experimental findings of a (2×1) reconstructed surface together with previous theoretical predictions [20] point toward a lanthanum terminated (2×1) surface reconstruction. Based on DFT, we performed an in-depth analysis of the electronic surface structure of such a (001) surface of LaB_6 with linear chains of lanthanum atoms at the surface, which are separated by void lines. This termination makes the surface formally charge neutral. Details about the DFT simulations, including the unit cell setup as well as technical

FIG. 7. DOS projected onto the d orbitals of the La surface atoms, resolved by magnetic quantum number. DOS data in arb. units. The individual contributions are stacked. Color code: Total DOS from La surface atoms (black), d_{xy} (gold), d_{yz} (orange), $d_{3z^2-r^2}$ (green), d_{xz} (red), $d_{x^2-y^2}$ (blue).

parameters, are given in Appendix B. Therein, we also present the relaxed surface structure.

The angular momentum projected density of states (DOS) obtained from our DFT surface calculation is shown in Fig. 6. For comparison, we show the orbital-projected DOS of a bulk simulation of LaB_6 which is in good agreement with previous DFT results [35,36]. In the data of the surface slab we find a characteristic peak -0.2 eV below the Fermi level, which is not present in the bulk data. This peak is a surface feature and is composed largely of states of boron and lanthanum atoms closest to the surface. The peak is made of boron dangling bonds sticking out of the surface, which bind to the La d_{xy} orbitals lying in the surface plane. The lobes of the d_{xy} orbital point towards the four adjacent boron dangling bonds. While the contributions of the La $d_{3z^2-r^2}$ and La $d_{x^2-y^2}$ orbitals are rather small within the peak, they are dominant in the energy intervals adjacent to the peak. The projection of the DOS onto the d orbitals of the La surface atoms is depicted in Fig. 7. For additional DOS projections, see Appendix B.

To connect our DFT simulations more closely to our STM/STS measurements, we follow Bardeen's tunneling theory [37] together with the arguments of Tersoff and Hamann [31,32], which relates the tunneling current for energies close to the Fermi level to the LDOS at the tip apex, integrated from the chemical potential of the probe to that of the tip.

Hence, to simulate the STM images, we compute the LDOS integrated over suitable energy windows. Rather than evaluating the LDOS at realistic tip positions, we choose a shorter distance of 4 Å above the plane of surface La ions. This is necessary, since at much larger distances the exponential decay of the LDOS leads to values that are too small to be resolved in our calculations. Furthermore, at 4 Å the contrast of the significant features is particularly clear. However, by comparing the images taken at 4 Å with images calculated at
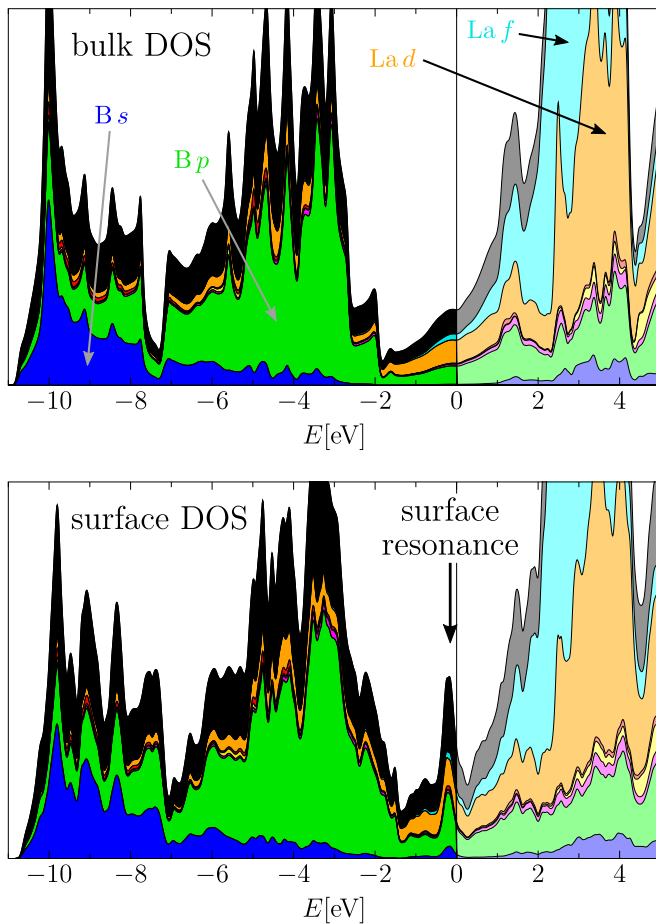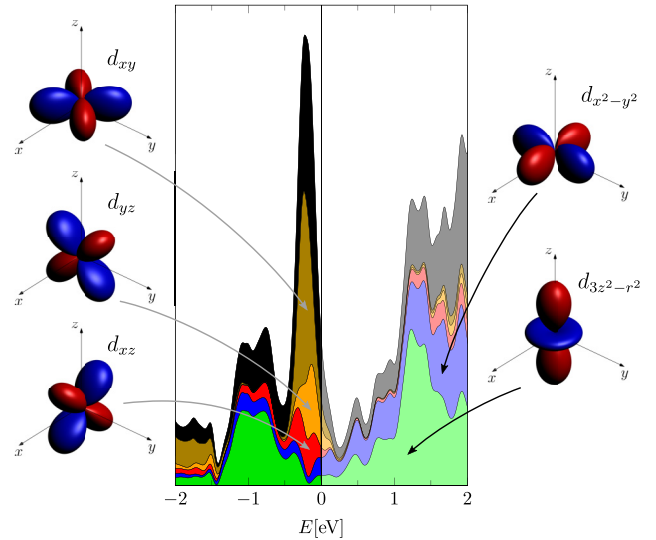

FIG. 6. Bulk DOS (top) and surface DOS (bottom) in arb. units projected onto atomic orbitals. The individual contributions are stacked. The Fermi energy is set to zero. Color code: Total DOS (not stacked, black), B s (blue), B p (green), B d (magenta), La s (yellow), La p (red), La d (orange), La f (cyan). The characteristic surface peak is indicated by an arrow.
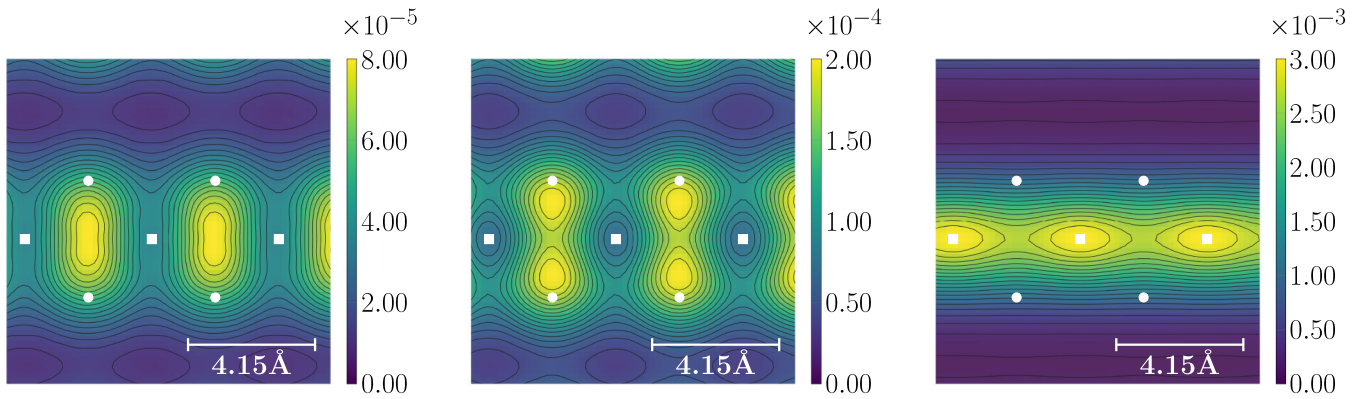
FIG. 8. Electron density at 4 Å above the surface for electrons from selected energy regions. Color scale in arb. units. Left: -1.29 eV to -0.53 eV, center: -0.53 eV to 0.28 eV, right: 0.28 eV to 1.64 eV. The white squares mark the positions of lanthanum atoms at the surface. White circles indicate the positions of the topmost boron atoms.

larger distances, we ensured that the contrast does not change qualitatively.

Figure 8 shows simulated STM images obtained from specific energy windows. At energies below E_F, the simulation images are dominated by the boron lone pairs (Fig. 8, left and middle graph). The contrast is especially clear in the energy window covering the characteristic peak in the DOS 0.2 eV below the Fermi level (Fig. 8, middle graph). While we observe distinct intensity maxima above the individual boron lone pairs in the energy window of the characteristic peak, we expect them to merge at larger distances, that correspond to realistic tip-surface distances.

The La ions are not visible in the energy windows below $E_F + 0.28$ eV, because the La d orbitals are more localized than the boron lone pairs. In addition, the nodal structures of the La d orbitals lead to a reduced density above the La ion in the range of the characteristic peak. This changes for the energy window above the characteristic peak at $E_F - 0.2$ eV: in the energy range from $E_F + 0.28$ eV to $E_F + 1.64$ eV, the La $d_{3z^2-r^2}$ orbitals pointing out of the surface contribute largely to the LDOS with the La f orbitals providing an

additional share. Hence the intensity is largest on top of the La positions.

To extract the local spectral information, which is provided by STS, we introduced so-called empty atoms above the surface. These atoms do not change the physics of the system, but they are a technical trick that allows us to extract the LDOS in the vacuum region. The empty atoms provide local orbitals onto which the wave functions are projected to obtain the projected DOS.

The LDOS projected onto layers of empty atoms is shown in Fig. 9. The characteristic peak of the boron dangling bonds below the Fermi level is very prominent. In addition, we find a second peak at $E_F + 0.47$ eV. As seen in Fig. 7, this peak is due to the $d_{3z^2-r^2}$ orbitals pointing out of the surface. At higher energies, in addition to the $d_{3z^2-r^2}$ orbitals, the f orbitals start to contribute to the LDOS.

Above the peak at $E_F + 0.47$ eV, the LDOS rises sharply. The rise of the DOS at higher energies can be attributed to two reasons: First, in this energy window the lanthanum ion has a large DOS due to d and f electrons. Second, wave functions at higher energies extend further out into the vacuum, because of their larger kinetic energy.

By comparing the LDOS at different distances, we find that the intensity of the dangling bond peak decreases faster with increasing distance than the intensity of the LDOS above the Fermi energy. This can be seen in Fig. 9.

IV. DISCUSSION

By investigating the lanthanum hexaboride (001)-cleavage plane in UHV conditions, we observed a chainlike (2×1) reconstruction. Our STM experiments show that these chains are mostly labyrinthlike arranged and the number of parallel chains barely exceeds three or four. The most ordered (2×1) reconstruction with a larger number of parallel chains can be found in the vicinity of step edges, where the chains tend to be ordered perpendicularly to the step edge. At a step edge which was rotated by $90°$, we observed the respective (1×2) reconstruction. Following these arguments, the observed (1×2) spots in the ULEED are likely caused by a step structure which was rotated by $90°$. This supports the assumption that
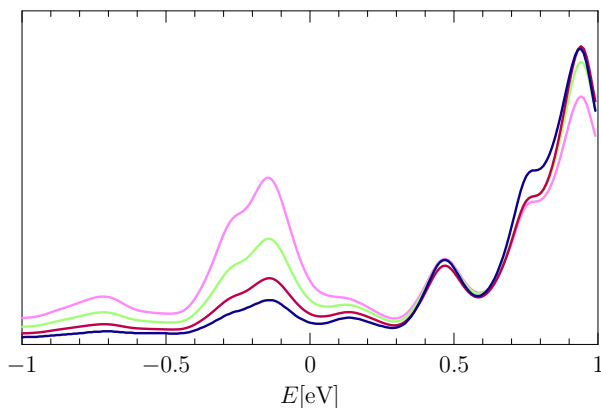

FIG. 9. DOS of the slab projected onto layers parallel to the slab at distances of 4 Å (pink), 5 Å (green, rescaled ×6), 6 Å (red, rescaled ×34), and 7 Å (blue, rescaled ×200) above the surface. The graphs are in arb. units.

the reconstruction aligns preferentially perpendicularly to step edges.

The atomic surface structure of the (2×1) reconstruction has been proposed as parallel lanthanum chains with a spacing of two lattice constants on top of a full B_6 layer [20]. Our DFT slab simulations of this lanthanum chain-terminated surface show that the electronic structure slightly below E_F is governed by a surface resonance. The orbital-projected DOS reveals that the surface resonance is mainly composed of boron sp-hybrid dangling bonds pointing out of the surface. In contrast, in the unoccupied states, La $d_{3z^2-r^2}$ orbitals are predominant. In comparison to the boron surface states, these orbitals show a slower decay and extend further into the vacuum.

Our simulated STM images provide a translation of these results to the language of CCT images recorded by STM experiments. On the one hand, the dominant contribution of the La $d_{3z^2-r^2}$ orbitals to the LDOS at $E > E_F$ leads to well-separated chainlike structures above the surface. This is in good agreement with our experimental CCT images, which were taken at positive bias voltages. Hence, at positive bias voltage, the STM addresses mainly the $d_{3z^2-r^2}$ orbitals. On the other hand, at $E < E_F$ or negative sample bias voltage, respectively, our theoretical results predict tunneling predominantly from the boron lone pairs to the STM tip. This is difficult to realize experimentally, since we find rather unstable tunneling conditions for negative bias voltages. Hence, imaging the surface at negative bias voltages remains an open task.

The presence of a spectral feature below E_F is, however, verified by our STS measurements. In the tunneling spectra, we find the surface resonance at $-0.6\,\mathrm{eV}$ and a parabola-shaped tunneling conductance around E_F. Experimentally, an additional feature is found at $0.1\,\mathrm{eV}$. These features would coincide with the calculated DOS if E_F was shifted by $+0.4\,\mathrm{eV}$ in the calculated DOS. We tested the dependence of the surface resonance position on the density functional by doing additional calculations with the PBE functional, i.e., without Hartree-Fock contribution. The peak position does not change. This can be rationalized from the nature of the state, which is mostly boronlike and has little La d and no La f contribution.

Although the investigated (2×1) structure is far from pristine and exhibits numerous kinks and defects, one can exclude that the surface resonance position depends on the presence of surface defects. Experimentally, we do not observe a shift of the surface resonance regardless of the local surface morphology, as seen in Fig. 12. Furthermore, the main features of the experimental tunneling spectra can be clearly identified in our DFT results on the defect-free surface.

A small shift in the chemical potential, which may explain the relative shift of 0.4 eV between experimental and theoretical spectra, could originate from a nonstoichiometric crystal. During crystal growth, preferential evaporation of boron atoms leaves the formed crystal slightly boron deficient [38]. Thus, the substance ratio La/B can be somewhat larger than the stoichiometric 1/6. For the present sample, the extra lanthanum atoms would lead to a surplus of charge carriers, shifting the Fermi level to higher energies.

The measured apparent barrier height is rather small with values in the range from 1 eV to 3 eV. This is in agreement with the low work function of about 2.5 eV obtained in former studies [8].

Moreover, the knowledge that the (2×1) reconstruction consists of lanthanum chains can be used to assign the termination of atomic steps. A step between two (2×1) reconstructed areas should be of integer multiple height of the bulk lattice constant, since the termination is equal on each side. Such steps have been observed. For the area shown in the left of Fig. 11, the step height is smaller than one bulk lattice constant. Here, we suggest a boron-rich termination with an almost vacant lanthanum layer at the surface. However, we would like to point out that this is one of the very few steps of that height we have found so far.

The surface morphology observed in this study is different to that of previous UHV STM investigations of LaB_6 [18,19]. In these studies, a (1×1) reconstructed (001) surface was found, which is stated to be lanthanum terminated and about 10% of the surface's lanthanum sites are vacant. However, it should be noted that the samples used in these studies are prepared by polishing and heating instead of cleavage as in our study, which likely leads to the different surface structures observed. Our structural results are more comparable to the findings on the cleaved surface of SmB_6. For cleaved SmB_6, surface step heights are only of integer multiples of the bulk lattice constant if the terminations on both sides are of the same kind [39], as observed in this study as well. Cleavage of SmB_6 can take place by breaking either the bonds within the boron octahedra or the bonds between the octahedra. Hence, it is lacking a natural cleavage plane [40–42], and atomically ordered areas occur rather infrequently [39,43]. Since LaB_6 has the same crystal structure, no natural cleavage plane is present. This might be the reason for the mostly disordered surfaces we have observed so far. Similar to our observations, LEED investigations on cleaved SmB_6 samples show only (2×1) spots on certain surface areas and the diffraction pattern is governed by (1×1) spots [44]. Therefore, the (1×1) spots have been associated with the bulk periodicity due to the finite penetration depth of the electrons. The same arguments should be applied for our sample system to explain the dominant (1×1) spots.

V. CONCLUSION

In a combined study of STM/STS, LEED, and DFT, we have investigated the (001)-cleavage plane of LaB_6. Atomically ordered areas are labyrinthlike (2×1) reconstructed. These chains can be understood as parallel rows of lanthanum atoms on top of a B_6 layer, with a surface resonance below E_F. Electronically, this resonance is mainly composed of B sp-hybrid orbitals and La d_{xy} states originating from the surface atoms. Lanthanum hexaboride is the electronically most simple candidate of the RB_6 family. However, understanding the electronic surface structure is not straightforward and differs severely from that of the bulk. Moreover, the LaB_6 surface morphology is more complex than previously discussed. Since all RB_6 have the same crystal structure, our findings could help to further understand the general surface physics of hexaborides.

APPENDIX A: SUPPORTING EXPERIMENTAL DATA

Figure 10(a) shows a typical large scale topography of the cleaved LaB$_6$ (001) surface as observed with AFM. Flat terraces within the AFM resolution with areas of several hundred (nm)^2 up to (μm)^2 in size can be easily found. These areas are connected by steps of integer multiples of the bulk lattice constant of 4.15 Å [20,46–51]. The steps in Fig. 10(a) are all of a height of one lattice constant. However, on a smaller length scale probed by STM, up to nanometer-sized protrusions with no pristine long-range order are commonly observed, Fig. 10(b). These results are similar to the STM findings on cleaved SmB$_6$ [39].

As described in the discussion above, LaB$_6$ is lacking a natural cleavage plane. If the cleavage leaves the boron cage intact, one dangling bond per octahedron is exposed. The situation changes dramatically if the cleavage proceeds through the octahedron. The disrupted boron cages expose numerous dangling bonds, which might increase the probability of attaching adsorbates like hydrogen [52]. Another reason for a frequently observed disordered morphology might be that the crystals were cleaved at room temperature. For SmB$_6$, it is reported that atomically flat surfaces could not be obtained by cleavage at room temperature, but only at about 20 K [53]. Our present setup does not allow the cleavage at cryogenic temperature. An additional experimental reason for the widely disordered appearance might be the tip itself. As seen in Fig. 2, even when atomic chains can be resolved, they are mostly labyrinthlike arranged. If the same area would
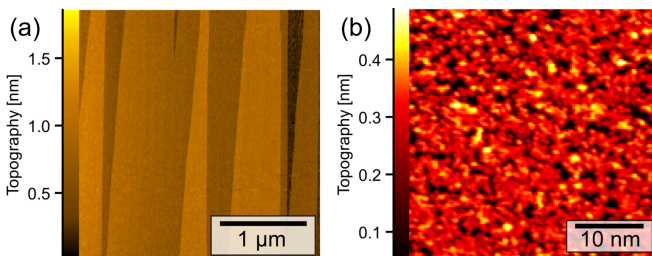

FIG. 11. (a) CCT image taken at 0.8 V/0.1 nA of two steps, one of about 1.3 Å height and one of a bulk lattice constant height, as shown in the height profile in (b).

have been scanned with a slightly blunt tip, the topography certainly would appear rather disordered, too.

We have found a step with a height of only a fraction of the bulk lattice constant, which is shown in Fig. 11. On the right-hand side, the already discussed (2 × 1) labyrinthlike structure is observed and the step height is again one bulk lattice constant. Interestingly, the step on the left-hand side is only about 1.3 Å high. We interpret this finding as a different surface termination, as described in the discussion above.

Figure 12 shows the spectroscopy of Fig. 5 again, but here including the measured apparent barrier height and another dI/dV(V, x) cross section. The mean value of the Φ_{app} map is (1.05 ± 0.17) eV. However, the specific value of the apparent barrier height is correlated with the topography. At the atomic protrusion, blue-marked position in Fig. 5(a), its value is about 1.1 eV and at the green-marked position 1.0 eV. For the various surface areas with no clear atomic rows included, the value of $\Phi_{app}(x, y)$ varies for each tip position.

Figure 13 shows the second spectroscopy data set, including the CCT, the $\Phi_{app}(x, y)$ map, and a dI/dV(V, x) cross

FIG. 12. (a) The CCT of Fig. 5 is shown again, this time with an overlay of the atomic lattice grid for scale. The blue arrows mark the lines along which the horizontal and vertical cross sections are taken. The resulting color coded dI/dV(V, x) maps can be seen in (c) and (d). In (b), the spatially resolved apparent barrier height is depicted.

FIG. 10. (a) (001) surface of cleaved LaB$_6$ as observed with AFM under ambient conditions. (b) CCT of a disordered surface area taken at 1 V/0.1 nA.
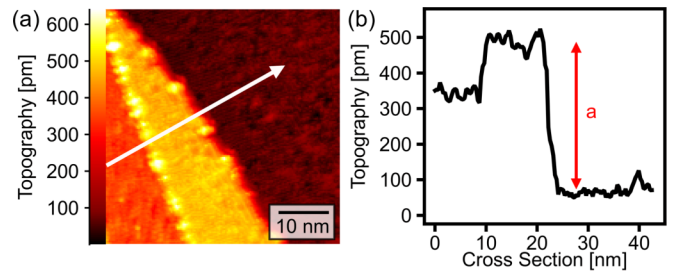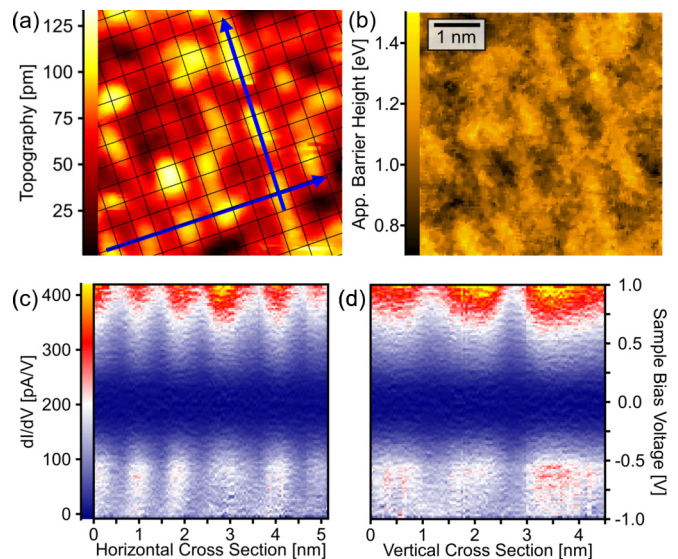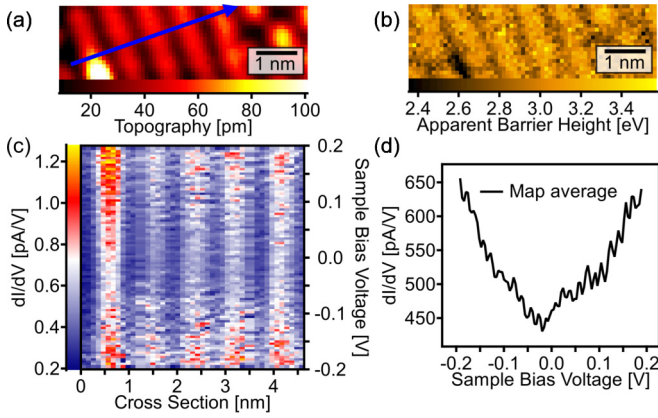
FIG. 13. (a) CCT taken at 0.2 V/0.1 nA. The apparent barrier height is shown in (b). The color coded $dI/dV(V, x)$ cross section taken along the blue arrow within (a) is depicted in (c). (d) shows the map averaged $dI/dV(V)$ curve of (a).

section after topography normalization. In this bias voltage range, the $dI/dV(V)$ curves have their largest values on top of the reconstruction's protrusion.

APPENDIX B: ADDITIONAL DETAIL ON THE DFT SIMULATIONS

A scheme of a simulated slab and its (2×1) surface unit cell is depicted in Fig. 14.

The lattice constant was kept fixed at a value of $a = 4.15 \, \text{Å}$ found in former experimental and theoretical studies [20,46–51]. The vacuum thickness between the slabs was set to 16.6 Å. To avoid artifacts and to have a sufficiently large spatial separation of the slab's top and bottom surfaces and surface states, respectively, a minimum slab thickness of three layers of boron octahedra is required. For our simulations, we used surface supercells with three, five, and seven layers of boron octahedra. This was done to ensure convergence of our DFT data with respect to the slab thickness. In this paper, we present results from our simulations with the seven-layer slab unit cell only. However, all slab thicknesses lead to similar results in atomic structure as well as electronic structure.

Moreover, we used a total amount of $8 \times 4 \times 1$ **k**-points. The plane-wave cutoffs were set to 50 Ry for the wave functions and to 100 Ry for the charge density. Furthermore,
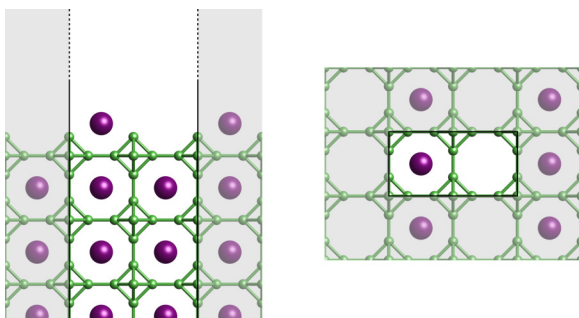

FIG. 14. Side and top view of the (001) surface of LaB_6. The slab unit cell is highlighted by a white background and marked with the black lines. On the surface only every second La row is filled.
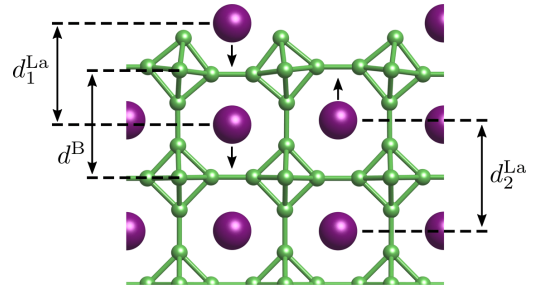

FIG. 15. Structure relaxation at the slab surface. d^{La} are distances between La atoms of the topmost layers as indicated. d^B is the distance between the centers of mass of the two octahedra. The small black arrows indicate the direction of the relaxation movement compared to the bulk structure.

we used (2,2,2,1) projector functions for the La (s, p, d, f) states and (2,2,1) projector functions for the B (s, p, d) states, respectively. The hybrid functional mixing factor was fixed at 0.15 for both atomic species.

In Fig. 15, we show the side view of the relaxed surface structure, which exhibits a tilt of the surface octahedra towards the filled chain of La ions. This can be rationalized by the attraction between positive La and negative B ions: The terminating boron atoms have lone-pairs pointing out of the surface, which hybridize with the La d_{xy} orbitals lying in the surface plane (cf. Fig. 7 and discussion in Sec. III C).

Furthermore, the surface relaxation leads to changes in the distance between two layers which can be quantified via the
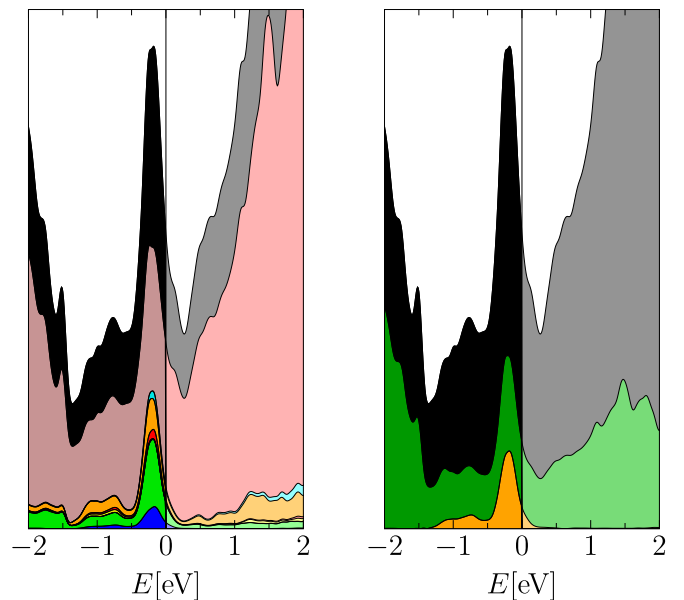

FIG. 16. Projections of the DOS onto orbitals of the surface layer atoms. DOS data in arb. units. The individual contributions are stacked. Left: DOS projected onto the topmost boron and lanthanum atoms. The color code is identical to the color code in Fig. 6. The bulk contribution is stacked on top (reddish brown). Right: DOS projected onto boron orbitals. The dangling bonds of the boron surface atoms (orange) dominate the peak close to the Fermi level. The contribution of all other boron orbitals of the slab (dark green) is shown for comparison.

relative change to the bulk lattice constant a_{bulk}, i.e.,

$$\Delta = \frac{d - a_{bulk}}{a_{bulk}}. \tag{B1}$$

The surface La ion relaxes inward by $\Delta_1^{La} = -4.3\%$ relative to the bulk, while the subsurface La ion below the empty La surface site relaxes outward by $\Delta_2^{La} = +4.7\%$. The boron octahedra exhibit a small outward relaxation of $\Delta^B = +1.4\%$. A comparison of these quantities between the data from the seven-B_6-layer slab to the data of the five-B_6-layer slab shows only minor differences which amount up to 0.007 Å in absolute values, which is negligible in the context of our calculations. Hence, we expect no significant difference in the DFT results for even larger slab thicknesses. Previous data published by Schmidt *et al.* [20] are $\Delta_1^{La} = -6.2\%$, $\Delta_2^{La} = +3.5\%$, and $\Delta^B = +0.4\%$, respectively. In comparison, the distances in our data are consistently a bit longer.

In Fig. 16, we provide two additional projections of the DOS: A projection onto the orbitals of the topmost atoms of either species, and a projection onto the boron dangling bonds.

[1] A. Takase, K. Kojima, T. Komatsubara, and T. Kasuya, Solid State Commun. **36**, 461 (1980).

[2] T. H. Geballe, B. T. Matthias, K. Andres, J. P. Maita, A. S. Cooper, and E. Corenzwit, Science **160**, 1443 (1968).

[3] T. Kasuya, Europhys. Lett. **26**, 277 (1994).

[4] S. Souma, H. Kumigashira, T. Ito, T. Takahashi, and S. Kunii, Physica B **312-313**, 329 (2002).

[5] M. Pohlit, S. Rößler, Y. Ohno, H. Ohno, S. von Molnár, Z. Fisk, J. Müller, and S. Wirth, Phys. Rev. Lett. **120**, 257201 (2018).

[6] M. Neupane, S.-Y. Xu, N. Alidoust, G. Bian, D. J. Kim, C. Liu, I. Belopolski, T.-R. Chang, H.-T. Jeng, T. Durakiewicz, H. Lin, A. Bansil, Z. Fisk, and M. Z. Hasan, Phys. Rev. Lett. **114**, 016403 (2015).

[7] H. C. Longuet-Higgins and M. De V. Roberts, Proc. R. Soc. London, Ser. A **224**, 336 (1954).

[8] M. Trenary, Sci. Technol. Adv. Mater. **13**, 023002 (2012).

[9] E. Sani, L. Mercatelli, M. Meucci, L. Zoli, and D. Sciti, Sci. Rep. **7**, 718 (2017).

[10] T. M. Mattox and J. J. Urban, Materials **11**, 2473 (2018).

[11] C. Oshima, E. Bannai, T. Tanaka, and S. Kawai, J. Appl. Phys. **48**, 3925 (1977).

[12] M. Aono, C. Oshima, T. Tanaka, E. Bannai, and S. Kawai, J. Appl. Phys. **49**, 2761 (1978).

[13] M. Aono, R. Nishitani, C. Oshima, T. Tanaka, E. Bannai, and S. Kawai, Surf. Sci. **86**, 631 (1979).

[14] L. W. Swanson and D. R. McNeely, Surf. Sci. **83**, 11 (1979).

[15] L. W. Swanson and T. Dickinson, Appl. Phys. Lett. **28**, 578 (1976).

[16] S. A. Chambers and L. W. Swanson, Surf. Sci. **131**, 385 (1983).

[17] B. Goldstein and D. J. Szostak, Surf. Sci. **74**, 461 (1978).

[18] J. S. Ozcomert and M. Trenary, Surf. Sci. **265**, L227 (1992).

[19] J. S. Ozcomert and M. Trenary, J. Vac. Sci. Technol., A **10**, 2581 (1992).

[20] K. M. Schmidt, O. Jaime, J. T. Cahill, D. Edwards, S. T. Misture, O. A. Graeve, and V. R. Vasquez, Acta Mater. **144**, 187 (2018).

[21] G. Balakrishnan, M. R. Lees, and D. McK. Paul, J. Cryst. Growth **256**, 206 (2003).

[22] G. Balakrishnan, M. R. Lees, and D. McK. Paul, J. Magn. Magn. Mater. **272-276**, 601 (2004).

[23] S. Vogelgesang, G. Storeck, J. G. Horstmann, T. Diekmann, M. Sivis, S. Schramm, K. Rossnagel, S. Schäfer, and C. Ropers, Nat. Phys. **14**, 184 (2018).

[24] P. Hohenberg and W. Kohn, Phys. Rev. **136**, B864 (1964).

[25] W. Kohn and L. J. Sham, Phys. Rev. **140**, A1133 (1965).

[26] CP-PAW website, http://www2.pt.tu-clausthal.de/paw/.

[27] P. E. Blöchl, Phys. Rev. B **50**, 17953 (1994).

[28] R. Car and M. Parrinello, Phys. Rev. Lett. **55**, 2471 (1985).

[29] M. Sotoudeh, S. Rajpurohit, P. Blöchl, D. Mierwaldt, J. Norpoth, V. Roddatis, S. Mildner, B. Kressdorf, B. Ifland, and C. Jooss, Phys. Rev. B **95**, 235150 (2017).

[30] J. P. Perdew, K. Burke, and M. Ernzerhof, Phys. Rev. Lett. **77**, 3865 (1996).

[31] J. Tersoff and D. R. Hamann, Phys. Rev. Lett. **50**, 1998 (1983).

[32] J. Tersoff and D. R. Hamann, Phys. Rev. B **31**, 805 (1985).

[33] J. K. Garleff, M. Wenderoth, K. Sauthoff, R. G. Ulbrich, and M. Rohlfing, Phys. Rev. B **70**, 245424 (2004).

[34] C. J. Chen, *Introduction to Scanning Tunneling Microscopy*, 2nd ed. (Oxford University Press, New York, 2008).

[35] M. A. Uijttewaal, G. A. de Wijs, and R. A. de Groot, J. Phys. Chem. B **110**, 18459 (2006).

[36] V. I. Ivashchenko, P. E. A. Turchi, V. I. Shevchenko, N. R. Medukh, J. Leszczynski, and L. Gorb, Physica B **531**, 216 (2018).

[37] J. Bardeen, Phys. Rev. Lett. **6**, 57 (1961).

[38] S. Otani, T. Aizawa, and Y. Yajima, J. Cryst. Growth **234**, 431 (2002).

[39] M. M. Yee, Y. He, A. Soumyanarayanan, D.-J. Kim, Z. Fisk, and J. E. Hoffman, arXiv:1308.1085v2 (2013).

[40] Z. Sun, A. Maldonado, W. S. Paz, D. S. Inosov, A. P. Schnyder, J. J. Palacios, N. Y. Shitsevalova, V. B. Filipov, and P. Wahl, Phys. Rev. B **97**, 235107 (2018).

[41] W. Ruan, C. Ye, M. Guo, F. Chen, X. Chen, G.-M. Zhang, and Y. Wang, Phys. Rev. Lett. **112**, 136401 (2014).

[42] C. E. Matt, H. Pirie, A. Soumyanarayanan, M. M. Yee, Y. He, D. T. Larson, W. S. Paz, J. J. Palacios, M. H. Hamidian, and J. E. Hoffman, arXiv:1810.13442v1.

[43] L. Jiao, S. Rößler, D. Kasinathan, P. F. S. Rosa, C. Guo, H. Yuan, C.-X. Liu, Z. Fisk, F. Steglich, and S. Wirth, Sci. Adv. **4**, eaau4886 (2018).

[44] S. V. Ramankutty, N. de Jong, Y. K. Huang, B. Zwartsenberg, F. Massee, T. V. Bay, M. S. Golden, and E. Frantzeskakis, J. Electron. Spectrosc. Relat. Phenom. **208**, 43 (2016).

[45] K. Momma and F. Izumi, J. Appl. Crystallogr. **44**, 1272 (2011).

[46] M. v. Stackelberg and F. Neumann, Z. Phys. Chem. **19B**, 314 (1932).

[47] X. Guo-Liang, C. Jing-Dong, X. Yao-Zheng, L. Xue-Feng, L. Yu-Fang, and Z. Xian-Zhou, Chin. Phys. Lett. **26**, 056201 (2009).

[48] C. H. Booth, J. L. Sarrao, M. F. Hundley, A. L. Cornelius, G. H. Kwei, A. Bianchi, Z. Fisk, and J. M. Lawrence, Phys. Rev. B **63**, 224302 (2001).

[49] N. N. Sirota, V. V. Novikov, V. A. Vinokurov, and Yu. B. Paderno, Phys. Solid State **40**, 1856 (1998).

[50] T. Gürel and R. Eryiğit, Phys. Rev. B **82**, 104302 (2010).

[51] F. M. Hossain, D. P. Riley, and G. E. Murch, Phys. Rev. B **72**, 235101 (2005).

[52] K. M. Schmidt, S. T. Misture, O. A. Graeve, and V. R. Vasquez, ACS Omega **4**, 65 (2019).

[53] S. Rößler, L. Jiao, D. J. Kim, S. Seiro, K. Rasim, F. Steglich, L. H. Tjeng, Z. Fisk, and S. Wirth, Philos. Mag. **96**, 3262 (2016).